Increased metamorphic conditions in the lower crust during oceanic transform fault evolution

Peter Haas[1], Myron Thomas[2], Christian Heine[3], Jörg Ebbing[1], Andrey Seregin[3], Jimmy van Itterbeeck[2]

[1]Institute of Geosciences, Christian Albrechts Universität zu Kiel, Kiel, Germany
5   [2]Shell International Exploration and Production B.V., Den Haag, The Netherlands
[3]Specialist Geosciences, Shell Global Solutions International B.V., Den Haag, The Netherlands

Correspondence to: Peter Haas (peter.haas@ifg.uni-kiel.de)

Abstract. Oceanic transform faults connect the segments of active spreading ridges that slide past each other. In a classical view, transform faults are considered as conservative, where no material is added or destroyed. Recent studies, however,
10   suggest that the crust in the transform fault region is deformed during different episodes. We combine high resolution 3D broadband seismic data with shipborne potential field data to study ancient fault zones in Albian-Aptian aged oceanic crust in the eastern Gulf of Guinea offshore São Tomé and Príncipe. The crust in this region is characterized by a thin, high-reflective upper crust, which is underlain by a thick, almost seismically transparent unit that comprises localized dipping reflectors, previously interpreted as extrusive lava flows. This layer defines the target area for inversion and forward modelling of the
15   potential field data. The picked seismic horizons are used as geometrical boundaries of the crustal model. First, we perform a lateral parameter inversion for the lower crust, which provides vertical columns of density and magnetic susceptibility. Second, we sort the estimated values using a clustering approach and identify five groups with common parameter relationships. Third, we use the clustered lower crustal domains to define a consistent 3D model of the study area that aligns with the seismic structure and geological concepts, preferred to the simple inversion of the first step. The final model shows anomalous low
20   susceptibility and medium to high density close to the buried fracture zones, which reflects increasing pressure and temperature conditions accompanied by a change of metamorphic facies. Our model indicates enhanced tectonic activity with an extensional component during the formation of oceanic crust that culminates in the transform region. These results are in line with recent studies and strengthen the impressions of a non-conservative character of ridge-transform intersections.

1 Introduction

Oceanic Fracture Zones (OFZ) are inactive remnants of ancient transform faults. Studies of transform fault processes are typically performed on modern crust at mid-oceanic ridges using bathymetric (e.g., Olive et al., 2015; Somoza et al., 2021; Olive et al., 2015), as well as seismic (refraction and controlled source, e.g., Keen and Tramontini, 1970; Lizarralde et al., 2004; Vaddineni et al., 2021), seismological (e.g., Rundquist and Sobolev, 2002; Schlindwein and Schmid, 2016), gravity (e.g.
30   Wessel et al., 2015) and magnetic data (e.g., Matthews et al., 2011). The density and susceptibility sources that generate the anomalies in the gravity and magnetic data, respectively, can be modelled to be located within the oceanic crust (e.g., Catalán et al., 2023; Osorio-Granada et al., 2022). In ancient buried ridge-transform settings, the distribution of these sources is complicated by the addition of sources within the overburden sediment pile. Yet, their distribution is important to understand the formation of transform faults and their transition to fracture zones. In this study, we investigate the density and magnetic
35   susceptibility structure of the oceanic crust in the eastern Gulf of Guinea, which hosts a set of buried Albian-Aptian aged fracture zones.

In the simplest view, transform faults are conservative plate boundaries where no material is added or destroyed. Strike-slip movement, generated at adjacent spreading ridges, displaces oceanic crust in opposing directions along vertical fault planes

(e.g., Wilson, 1965). Recent studies suggest a more complex interaction between ridge segments and transform faults. Indeed,
gravity anomalies (i.e. residual mantle Bouguer anomalies) along transform faults show a correlation with spreading rate of
the adjacent mid-oceanic ridge (Gregg et al., 2007). This suggests a mass deficit underneath fast-slipping transform faults
compared to adjacent ridge segments, which could indicate crustal thickening of magmatic material close to fast-slipping
transform faults (Gregg et al., 2007). Contrary, a recent study shows a systematic shallower crust underneath transform faults
than adjacent fracture zones (Guo et al., 2023). These studies primarily use potential field data for crustal thickness estimates,
but are unable to distinguish the internal density structure of the crust, which causes the observed signals.

3D plastic shear-based numerical modelling showed that the inside corner between ridge and transform may not be purely
conservative, but can be accompanied by oblique shear and horizontal extension (Grevemeyer et al., 2021). Interpretation of
3D seismic reflection data offshore São Tomé and Príncipe of Albian slow spreading crust provided observational evidence
for the oblique shear model, where the inside corner of the ridge-transform intersection acts as a conduit for decompression
melt and volcanism (Thomas et al., 2022). Growth packages of extrusive lavas termed Transform Normal Dipping Reflectivity
(TNDR packages), thickened towards the transform fault and record extension and crustal detachment. A basal 35° dipping
bounding surface, the TNDR-B, limits the TNDR package and terminates down onto the Moho. The TNDR-B was interpreted
as a crustal scale detachment fault, which likely provides a conduit for melt feeding the TNDR lava packages. Sealing of the
TNDR packages by abyssal hills geometries dates this process to be a transform fault process. If such processes are common,
then TNDR packages are expected to leave signatures in density and magnetic properties, which contrast to the adjacent
'typical oceanic crust', and therefore should be seen in potential field data.

Combining high-resolution seismic data with potential field data provides the opportunity to reveal the internal architecture
and complexity of fracture zones and adjacent crustal segments (e.g., Antobreh et al., 2009; Marjanović et al., 2020). Here, we
combine published seismic observations, including the TNDR packages, with shipborne potential field data to model the
density and susceptibility structure of the crust in São Tomé and Príncipe. Our results reveal distinct anomalies in the vicinity
of OFZ and TNDR packages that differentiate them from the surrounding oceanic crust.

2 Study area

São Tomé and Príncipe is located in the Gulf of Guinea, offshore West Africa. The study area is situated in the territorial
waters of São Tomé and Príncipe and to the west of Gabon (Fig. 1). The bathymetry is characterized by a gentle ascent towards
the passive margin, ranging from 3000 meter below sea level (mbsl) in the most offshore part in the southwest up to
approximately 2350 mbsl close to the Landward Limit of Oceanic Crust (LaLOC) (Fig. 1).

To the west of the study area, the islands of São Tomé and Príncipe are the result of major Neogene volcanism along the
Cameroon Volcanic Line (CVL) (Lee et al., 1994). A few sills intruded into the sedimentary overburden and recognized in the
3D seismic in the south of the study area are the only indications of the CVL within the study area. Nevertheless, previous
potential field studies in the basin have focussed on the CVL structure in relation to upper mantle processes and the uplift of
oceanic crust (Meyers et al., 1998; Wilson et al., 2003). The timing of the CVL significantly post-dates the Albian aged oceanic
crust and is not discussed in this study.

The Global Seafloor Fabric Data Base (Matthews et al., 2011) shows a series of OFZ close to, but outside of the study area
(Fig. 1). The Ascension Fracture Zone (FZ) in the south and the Bata FZ in the north come closest to the survey outline. High
resolution broadband 3D seismic data used in this study map the Bata FZ further south, inside the NW part of the study area,
and the Ascension FZ in the southern part of the study area. The Ascension FZ extends close to the LaLOC and is a feature
that is not captured in the global data compilation. Additionally, a third SE-NW trending fracture zone is mapped on 3D seismic
data, crossing the central part of the study area and was termed the "Central Fracture Zone" (Thomas et al., 2022).

The LaLOC is situated within a few tens of kilometres to the east of the study area and contains strong right lateral offsets,
80   which approximately reflect the terminations of the mapped OFZ (Thomas et al., 2022). The abyssal hills fabric is observed
on the seismically mapped Top Oceanic Crust with a northwest-southeast trending ridge fabric in accordance with the
perpendicular orientation of the fracture zones and recording a southwest-northeast oriented spreading direction. The study
area therefore lies exclusively on oceanic crust.

Precise dating of the age of the oceanic crust in the study area is difficult, due to an age within the range of the Cretaceous
85   Normal Superchron (CNS) (Granot et al., 2012) and lacking direct control through wells. The closest isochron is the young
end of C34n (83.5 Ma) (Heine et al., 2013; Ogg, 2020). While magnetic anomaly identifications and global oceanic crustal
age models map the age of the crust between 110-120 Ma (Seton et al., 2020), plate kinematic model-derived ages suggest a
formation age between 105-110 Ma (Heine et al., 2013). Discrepancies are partly reflected in the age grid misfit of the global
model (Seton et al., 2020), choices of the location of the LaLOC and plate kinematic models used. Disregarding the exact age
90   of the oceanic crust, the absence of magnetic stripe patterns hampers precise assumptions on remanent magnetization. In
agreement with the present day Mid-Atlantic ridge, the rugosity of the oceanic crust within the study area indicates slow to
moderate spreading velocities, which are in line with plate kinematic model predictions (Thomas et al., 2022; Heine et al.,
2013).
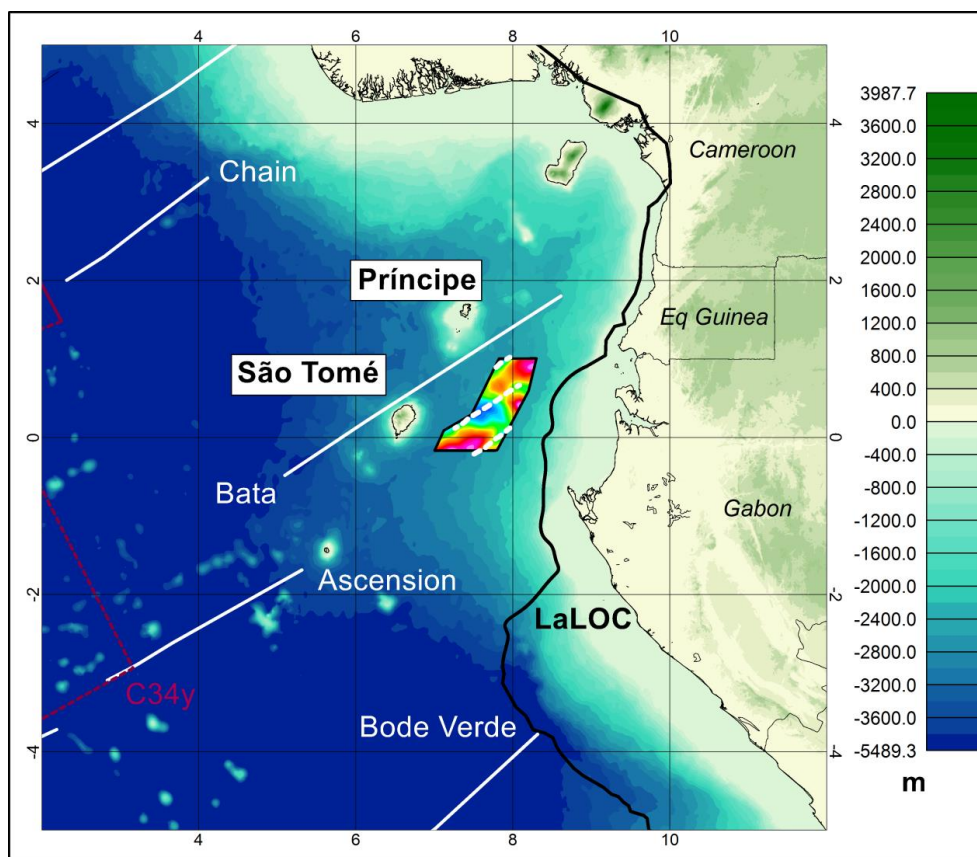
95   **Figure 1: Bathymetry of the Gulf of Guinea, taken from GEBCO. The study area offshore São Tomé is highlighted by colour-filled
polygon. Solid white lines indicate OFZ, taken from the global seafloor fabric data base (Matthews et al., 2011). LaLOC= Landward
Limit of Oceanic Crust (taken from Heine et al., 2013). Dashed white lines define the fracture zones mapped with 3D seismic data
(Thomas et al., 2022). Dashed dark line indicates Magnetic Chron C34y at 83 Ma, taken from Heine et al. (2013).**

3 Data and Methods

The seismic, marine gravity and magnetic data used in this study were acquired simultaneously in a survey area of ca. 16,050 km^2 by the M/V Oceanic Endeavour. The survey was conducted by CGG Multi-Physics and lasted from January to August 2017. During this period, 23,886 km of gravity and 23,960 km of magnetic data were collected with individual profile spacing of approximately 600 m. For this study, a subset of the data is available, covering an area of 8,000 km² (Fig. 1).

3.1 Gravity and magnetic data

Gravity and magnetic data processing was performed by CGG Multi-Physics and consisted of several key stages, which are described in this section.

For the gravity data, instrument drift was calibrated by five still readings. Earth tide correction was calculated using the formulas given in Longman (1959). This correction was calculated on a by point-by-point basis and added to the calibrated gravity. The Eötvös effect, which occurs when measuring gravity on moving a platform (Harlan, 1968), was corrected using a time-varying decorrelation procedure, which presumes that correlation existing between observed gravity and the computed Eötvös effect is the true Eötvös effect, allowing removal.

In a next step, the Free Air Anomaly was calculated by subtracting the theoretical GRS 1980 gravity value from the pre-processed value. No height correction was applied, as the observation height above the spheroid is assumed to be zero. Further, the gravity data were levelled and gridded with 200 m distance using the prediction gridding technique, which reduces the noise level for high-resolution potential field data. Subsequently, a 2000 m Butterworth low-pass filter was applied to eliminate extraneous noise without removing valid signal information. Figure 2a shows the gridded Free Air Anomaly of the study area, which serves as input for the inversion of the crustal density.

For the magnetic data, an IGRF-correction (International Geomagnetic Reference Field) was applied. The Earth's nominal magnetic field was computed for every sample point using the location and time of the point and the 12th Generation International Geomagnetic Reference Field (IGRF-12) formula, updated to the survey dates. Further, CGG obtained base station magnetic data from the Ascension Island Geomagnetic Observatory, which is approximately 2,600 km SW of the survey area, and from the Yaounde Geomagnetic Observatory in Cameroon. Base magnetometer data was decorrelated from the recorded magnetic data to remove diurnal effects. After levelling the individual line data, the magnetic data was gridded with 200 m distance (Fig. A1).

As input for the inversion, reduction-to-pole (RTP) was applied to the magnetic data. This operation aims to aid interpretation of magnetic data by transforming observed magnetic anomaly data as if it was acquired at the magnetic pole with vertical geomagnetic inclination. As a result, magnetic anomalies are expected to be located directly above the causative magnetic sources. Geomagnetic inclination of -29.1° and declination of -2.59° were used as average parameters for the survey area to generate RTP magnetic anomaly grid.

Application of the RTP correction to magnetic data that is acquired at low magnetic latitudes is unstable and might lead to numerical artifacts like streaks in the data in declination direction (e.g., Stewart, 2019). Even though the study area offshore São Tomé is located close to the equator, the background magnetic inclination is -29.1°, which limits the expected artifacts of RTP correction at low inclinations. Furthermore, noise in the acquired data is one of the main factors that causes linear artifacts along the direction of the declination (Li, 2008). Such anomalies are not observed in the magnetic data used for the study after the RTP correction (Fig. 2b) and therefore, the selected data set is suitable for investigating the susceptibility of the lower crust.
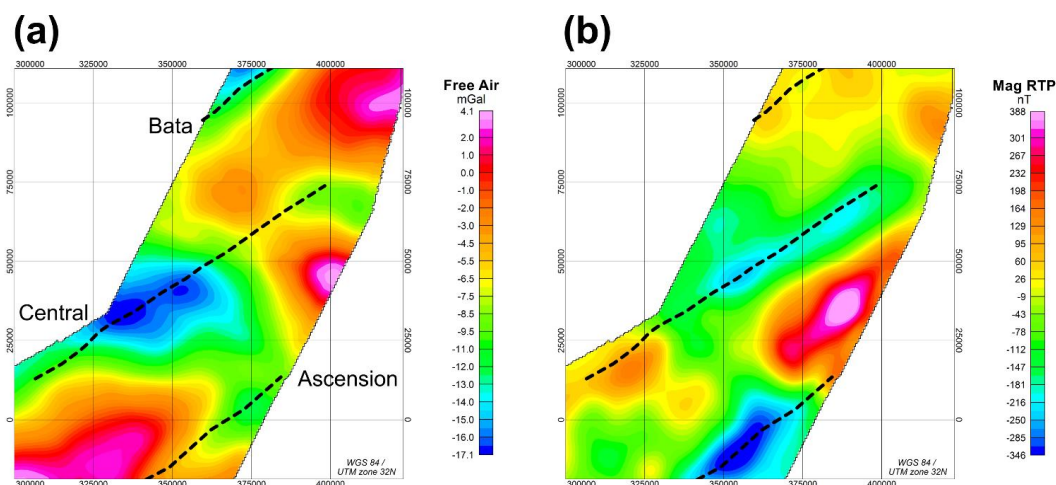
Figure 2: (a) Free air gravity anomaly, (b) RTP magnetic anomaly. Dashed lines indicate OFZ in the study area, taken from Thomas et al. (2022).

3.2 Seismic data

The seismic data set is a broadband 3D acquisition with a shot spacing of 25 m. Details of the acquisition and processing workflow can be found in Thomas et al. (2022). Thomas et al. (2022) utilized a Kirchoff PreStack Depth Migration providing a more reliable placement of reflectors and amplitudes, but with a limited 12 km processed depth limit. A simple Gaussian Beam migration provided a lower resolution migration, but to the full 18 seconds Two-Way Time (TWT) record length, such that the entire Moho and part of the upper mantle are included (Fig. 3). For this study, crustal seismic interpretation from the Kirchoff migration (Thomas et al., 2022) is combined with observations and Moho interpretation from the Beam migration.

The 3D seismic data is used to provide a series of discrete dip line geotiffs, oriented perpendicular to the fracture zones (Fig. 4). In addition, several seismic horizons mapped on the 3D seismic and published in Thomas et al. (2022) are used to define the boundaries between different crustal units. These boundaries comprise the water bottom (Fig. 4a), Top Oceanic Crust (Fig. 4b), base of Unit 2 (Fig. 4c) and the Moho (Fig. 4d). The events are provided in depth using a PreStack Depth Migration velocity model, generated during the data processing workflow (see Thomas et al., 2022 for details).

Unit 2 of Thomas et al. (2022) is the uppermost layer of oceanic crust, defined as containing horizontal to subhorizontal high amplitude reflectors with a lateral continuity of 2 to 5 km. It is interpreted as a mixture of extrusive lavas and sediments. The base of Unit 2 horizon therefore separates this portion from the transparent seismic facies which makes up the lower crust (Fig. 3). For details of the seismic stratigraphy the reader is referred to the study of Thomas et al. (2022).

Five TNDR-B detachment surfaces from within the fracture zones are also included in the model and are labelled 1 through 5. As defined in the introduction, these detachment surface link the Moho to the Top Oceanic Crust and mark a key lateral boundary between 'standard' oceanic crust and the TNDR packages of the FZ. Their planform outlines are also included (Fig. 4b). The mapped locations of the fracture zones (Fig. 2 and 4) are derived from FZ topographical scarps on the Top Oceanic Crust horizon (Fig. 4b).
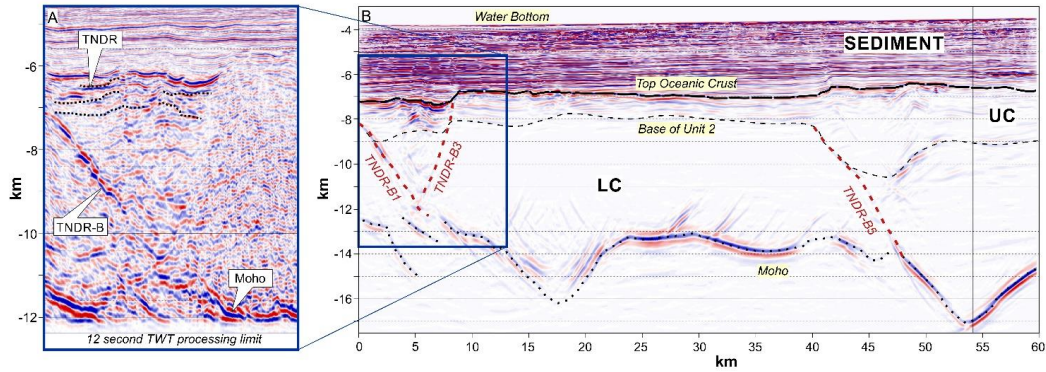
Figure 3: Seismic Dip Line equivalent to geotiff location 5 (see Fig. 4 for location). UC= Upper Crust, LC= Lower Crust. Solid lines mark the bounding horizons between the layers. Dashed ellipses define areas of increased reflectivity in the lower crust (TNDR-B horizons). The seismic line is labelled in 5 km distance increments starting on the western side (Fig. 4).
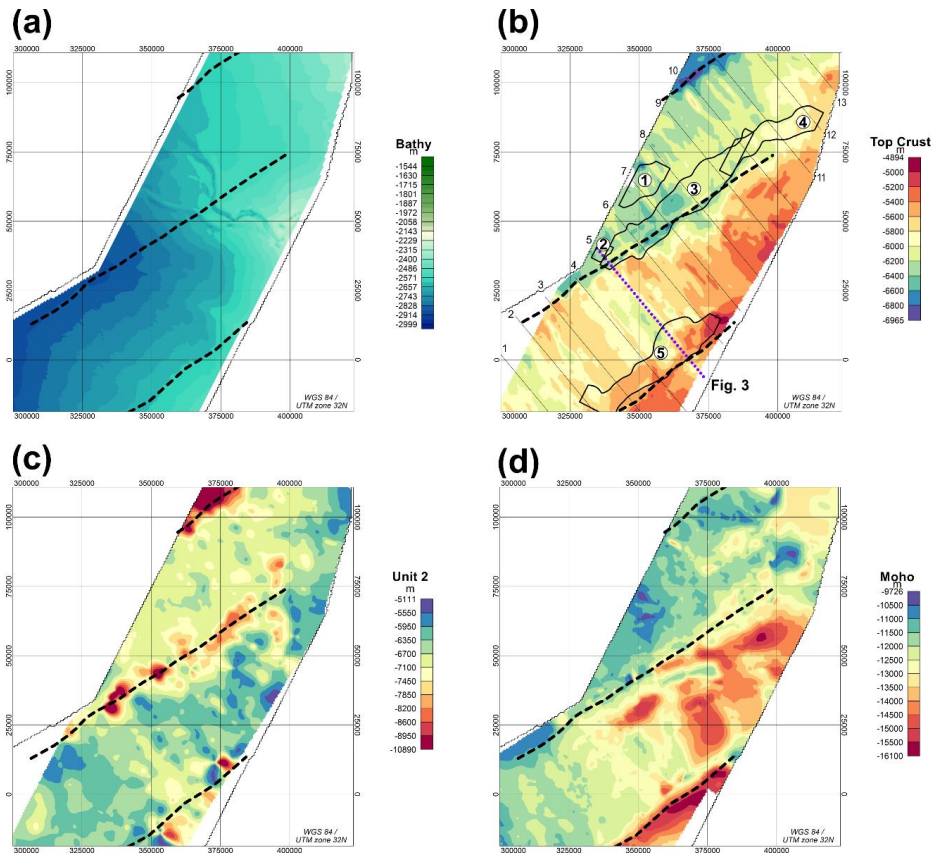
Figure 4: Depth of seismic horizons that are used as geometrical constraints for the crustal model. (a) Bathymetry, (b) Top Crust, (c) Unit 2, (d) Moho boundary. Horizons are taken from the study of Thomas et al. (2022). Thick dashed lines indicate OFZ. Panel (b) shows additional structural data. Black polygons define the extension of the TNDR-B surfaces, labelled from 1-5 according to Thomas et al. (2022). Thin solid lines indicate section locations, which are used to define the model in IGMAS+ (see Sect. 3.3), labelled from 1-13. Dotted violet line defines the seismic cross-section shown in Fig. 3.

3.3 Defining the crustal model

175

The boundaries shown in Fig. 3 are implemented in GM-SYS 3D, part of Oasis Montaj, which is a gravity and magnetic modelling software for layered-earth models. As an extension, GM-SYS 3D allows the lateral inversion for density and susceptibility of selected crustal layers. Calculations of the potential fields in GM-SYS 3D are performed in the wave number

180 domain based on the Parker Algorithm (Parker, 1973). Here, we make use of this software and invert the gravity and magnetic data to obtain a first-order density and susceptibility model of the crust.

Particularly, we focus on the crustal material between Base of Unit 2 and Moho, which we define as the lower crust of the model. The lower crust forms > 80 % of the crustal thickness and contrasts to the overlying high-amplitude reflectors (Fig. 4). In addition, it provides the space for the TNDR-B surfaces to detach on the Moho boundary. Therefore, the main gravity and

185 magnetic sources are expected to be located in this layer.

The densities and susceptibilities of the layers are shown in Table 1. For the lower crust, the values represent starting parameters prior to the inversion. During the inversion, the lateral densities and susceptibilities are iteratively updated, until the misfit between the observed and modelled gravity and magnetic data reaches a user-defined threshold. We define thresholds of 1 mGal for gravity data and 10 nT for magnetic data, respectively. Several starting susceptibilities of the lower crust were

190 tested to investigate the distribution of the inverted lateral susceptibility. We selected a starting susceptibility of χ=0.15 for the lower crust, as this represents the lower threshold to avoid negative susceptibilities in the inverted model. For the densities of the sediments, we apply a calibrated mudrock density-depth trend based on available well log data (pers. comm.):

$$\rho_{sed}=2.00+0.00123448 \cdot z_{bml}^{0.7359959}, \tag{1}$$

where z_{bml} is depth below mudline.

195 This gives sediment density values in a range between 2.0 to 2.56 g/cm³.

After inverting for the density and susceptibility of the lower crust separately, we use a clustering approach to differentiate geological units with similar properties. This allows us to investigate if gravity and magnetic data are sensitive to similar sources. Previous studies have interpreted density and susceptibility grids by cross plot analysis with 2D colour scale (e.g., Fichler and Pastore, 2022) or Gaussian Mixture Models (e.g., Lösing et al., 2022). Here, we apply the latter algorithm to the

200 inverted fields and define a certain number of clusters, depending on the distribution of the parameters. These clusters represent different lower crustal types.

In a next step, the laterally variable lower crustal lithologies are implemented together with the bounding horizons, as well as the TNDR-B surfaces in IGMAS+ (Götze and Lahmeyer, 1988; Anikiev et al. 2020). IGMAS+ is a software for 3D numerical modelling and interdisciplinary interpretation of potential fields. Compared to GM-SYS 3D it allows a more independent

205 implementation of additional constraints and is therefore well-suited to transform the vertical blocks of the inverted lower crust into a 3D geometry, which better links the model structure to the 3D seismic observations and thus better represents geological plausibility.

We define 13 cross-sections with a separation distance of approximately 10 km (Fig. 3a). The cross-sections are oriented oblique to the fracture zones in order to best capture the transition from the oceanic crust to the high reflective crust close to

210 the fracture zones. Densities and susceptibilities of the lower crust are modelled to fit the measured potential field data, but are limited in the range of the obtained cluster types. Distinct reflectivity in the seismic dip lines was used as a proxy to define the geometry of the TNDR packages.

Layer	Basal bounding horizon	Density [g/cm³]	Susceptibility [SI]
Water	Water bottom	1.0	0

Sediments	Top Oceanic Crust	2.0-2.7[1]	0
Upper Crust	Base of Unit 2	2.7	0.095
Lower Crust	Moho	2.9[2]	0.15[2]
Mantle Lithosphere	100 km constant	3.3	0

Table 1: Densities and susceptibilities of the five layers of the model. [1]Depth-dependent density, [2]Starting values prior to inversion.

215

4 Results

The inverted density of the lower crust shows a variable distribution (Fig. 5a). More than 95 % of the inverted density, which corresponds to twice the standard deviation 2σ, is ranging between 2.82 and 3.02 g/cm³ (Fig. 5a) and reflects expected lower crustal lithologies of basaltic and gabbroic materials (Dentith and Mudge, 2018). Peak values up to 2.61 in the lower limit and

220   3.19 g/cm³ in the upper limit are found only at the edge of the model and might represent artifacts caused by extrapolating the data as a preparatory step for the Fourier transform. Figure 5 also shows the outline of the TNDR-B surfaces, which are only found in the vicinity of the fracture zones (Thomas et al., 2022). Densities higher than 2.96 g/cm³ nucleate in those areas, where the two large surfaces TNDR-B 3 (Central FZ) and TNDR-B 5 (Ascension FZ) occur.

The inverted susceptibilities show strong variations with values higher than 0.2 SI in the NW and SW of the model and lowest

225   values below 0.05 SI in the SE of the model (Fig. 5b). Compared to density, the inverted susceptibilities extend up to the outermost range of crustal lithologies. Particularly, susceptibilities > 0.24 SI in the NW part (dark red colours in Fig. 5b) can only be expected for highly magnetic gabbros (Dentith and Mudge, 2018). The high susceptibility of the lower crust might indicate missing magnetization in the upper crust. However, the upper crust is much thinner than the lower crust and therefore, increased susceptibility of the upper crust does not significantly change the inverted susceptibility of the lower crust (Fig. A2).

230   More likely, the high susceptibilities at the edge of the model reflect an artificial pattern, where the inversion tries to fit anomalies that are not fully covered in the data set. For structural interpretation we will not consider these high susceptibilities, as the TNDR-B sequences are rather located in the central and SW part of the model. Here, lower magnetization is found. Particularly, the Ascension FZ and the adjacent TNDR-B 5 surface reveal susceptibilities close to zero, implying almost magnetically transparent crustal material, which is investigated below in the discussion section.

235
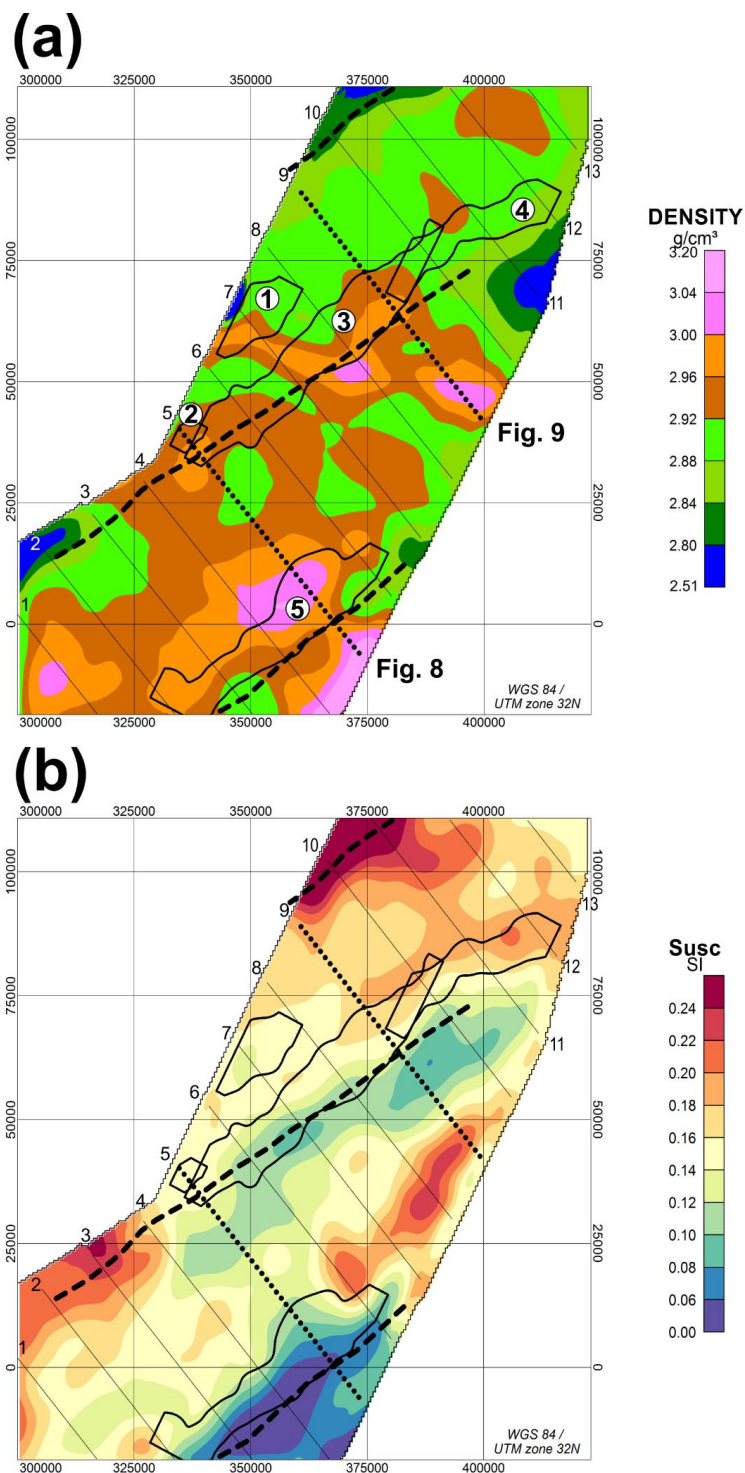
Figure 5: Inverted densities (a) and susceptibilities (b) of the lower crust. Thick black dashed lines indicate fracture zones. Polygons mark the extent of the TNDR-B surface, taken from Thomas et al. (2022). Encircled bold numbers indicate the respective number of the mapped TNDR-B, according to Thomas et al. (2022). Dotted lines indicate cross-sections that are shown in Fig. 8 and 9. Regular numbers indicate the labels of the seismic cross-sections.

240

In the next step, the inverted densities and susceptibilities are investigated with the Gaussian Mixture clustering algorithm (e.g., Lösing et al., 2022). This gives a first impression, how the sources of the inverted fields are related to each other. Given the simplicity of the utilized inversion approach, the distribution of the inverted parameters shows clear structures that can be attributed to certain clusters.

245

We define five lower crustal clusters C1-C5, as this number coincides with well-defined segments of density and susceptibility (Fig. 6): The highest frequency group C1 shows medium density and medium susceptibility, varying between 2.85-3.0 g/cm³ and 0.15-0.24 SI, respectively (statistical values are denoted in Table 2). Two other groups are defined by high density between 2.90-3.05 g/cm³ and medium susceptibility (C2), as well as a cluster with a broad range of density, combined with a

250

comparatively narrow range of low susceptibility between 0.08-0.14 SI (C4). Furthermore, the distribution shows two distinct arms, which are clustered as a combination of low density and high susceptibility (C3), as well as high density and very low susceptibility (C5). C3 contains the high susceptibilities at the NW edge of the study area, mentioned previously. In contrast to that, C5, together with C4, are located along the Ascension and Central FZ and their respective TNDR packages (Fig. 6b). The combination of a high density and low magnetic lower crust becomes especially evident in the vicinity of the Ascension

255

FZ (Fig. 6b). The distribution of the individual TNDR packages is shown in Fig. A3. There is also statistical evidence that the TNDR sequences, especially TNDR 3 and TNDR 5, preferably represent a medium-high density and low susceptibility compared to the surrounding lower crust, which is represented in the clusters C4 and C5. This is evident by calculating the cluster distribution within the respective TNDR-B polygons (Table A1).
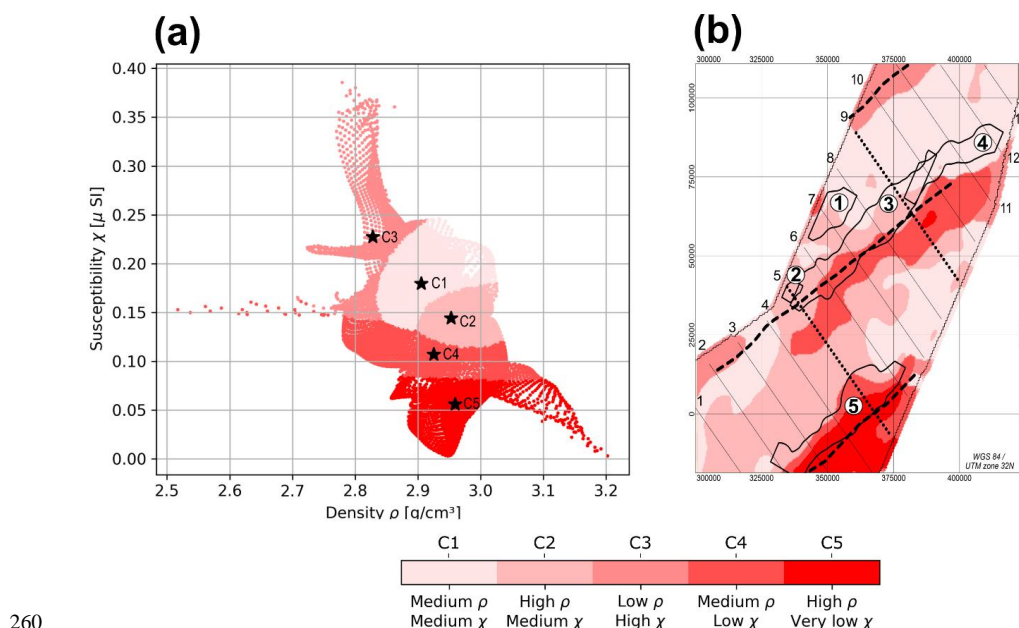
260

Figure 6: Clustered density and susceptibility of the lower crust. (a) Density vs. susceptibility plot. Stars mark the average values of the respective cluster centers (Table 2). (b) Estimated clusters shown on a spatial map. Polygons and numbers indicate the extension of the TNDR sequences. Regular numbers indicate the labels of the cross-sections.

Cluster	Average density ρ [g/cm³]	Average susceptibility χ [SI]

C1 – Medium ρ, medium χ	2.91 ± 0.03	0.180 ± 0.020
C2 – High ρ, medium χ	2.95 ± 0.03	0.144 ± 0.013
C3 – Low ρ, high χ	2.83 ± 0.03	0.227 ± 0.052
C4 – Medium ρ, low χ	2.93 ± 0.06	0.107 ± 0.012
C5 – High ρ, very low χ	2.96 ± 0.06	0.056 ± 0.020

265 **Table 2: Average values and standard deviations of density ρ and susceptibility χ for the different clusters.**

The estimated clusters are utilized as structural constraints to define crustal blocks within the model that are geologically plausible and correspond to the seismic horizons and interpretation of Thomas et al. (2022). Together with the other layers, the cluster derived blocks are located on the 2D cross-sections and connected to a 3D model in IGMAS+. The model itself is
270 defined from the surface to 100 km depth and therefore captures mantle lithosphere and asthenosphere (Fig. 7). The properties of the lower crustal blocks are allowed to vary laterally, but must be constant for connected bodies. The range of possible variation of density and susceptibility is limited by the respective standard deviations, as listed in Table 2. For example, Lower Crust C1 along sections 6-10 in the NW part of the model may have different properties than Lower Crust C1 along sections 1-4 in the southern part. As an addition, the TNDR-B surfaces are incorporated in the model. Similar to the other bodies, their
275 properties are constrained by the standard deviations (Fig. A3). In the 3D IGMAS model, the TNDR packages are recognized as lenticular structures that are clearly differentiated from the surrounding vertical blocks of the lower crust (Fig. 7).
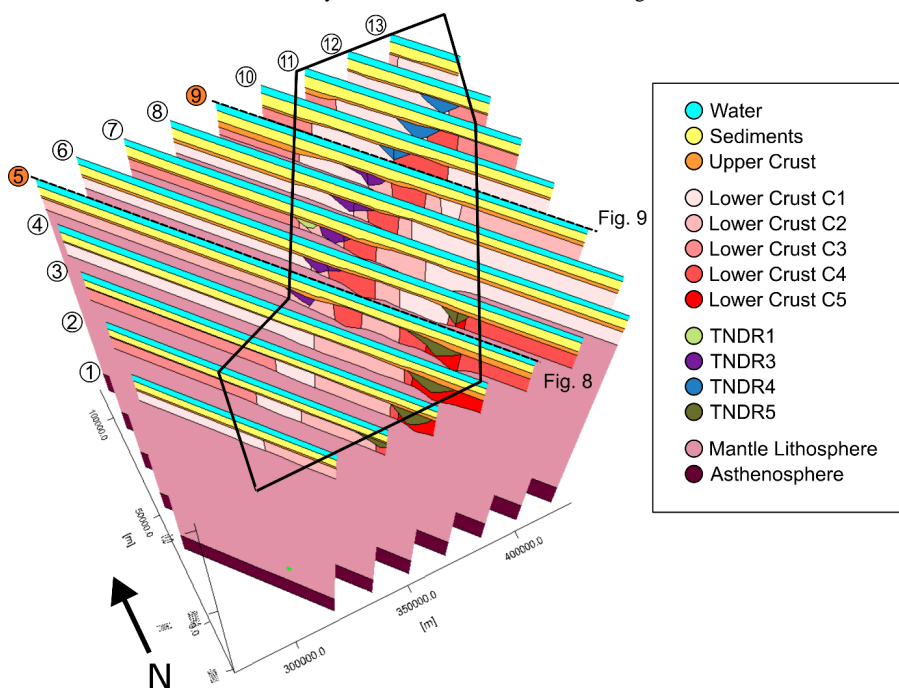
Figure 7: 3D IGMAS model with cross-sections, labeled from 1-13, that define the 3D geometry of the model. Sections 5 and 9 (Fig. 8 and 9) are highlighted with orange colour. Black polygon defines the boundary of the study area. The geometry of the five lower
280 **crustal bodies is taken from the clustered domains. Note that the TNDR-B 2 surface is too small to be resolved in the model.**

Two representative 2D seismic sections are selected to demonstrate the crustal structure along the Ascension and Central FZ and their respective TNDR packages. Each discrete seismic line is labelled in 5 km distance increments starting on the western side. The first cross-section, Section 5, captures the surface extension of the Ascension FZ and the related TNDR 5 package in the SE part of the profile, as well as the onset of the Central FZ with a smaller package of TNDR 3 towards NW (Fig. 8).

285   Strongest reflections occur along the Moho boundary in the central and SE part of the profile (Fig. 8d). Toward the NW the reflectivity of the Moho boundary becomes more indistinct and vanishes with the onlapping TNDR 3 package.

In the SE, high crustal densities are modelled for the TNDR 5 and the adjacent lower crustal domains (Fig. 8c). The density of the TNDR 5 volume only differs slightly from the surrounding lower crust, which is also correlated with poor reflectivity inside the lower crust. Contrary, the low susceptibility of the TNDR 5 reflects a sharp contrast to higher susceptibilities of the

290   adjacent lower crustal body of cluster C4. Towards the west, a smooth transition to higher susceptibility and lower density is modelled associated with missing lower crustal reflectors. Pronounced lower crustal reflectors between 0-5 km of the profile mark the onset of the TNDR-B 5 surface and are modelled with an anomalously low density of 2.89 g/cm³, which marks the lower boundary of the expected density range obtained from clustering.

The predicted signal generally matches with the observed trend of the gravity and magnetic data. The data mismatch of 0.7

295   mGal reflects the allowed range for the properties of the lower crustal bodies. Enhanced reflectivity in the upper crust between 5-10 km markers of the profile and 6-8 km depth could indicate a change of crustal properties. Such small-scale lateral variations in the upper crust could also explain the mismatch in the magnetic data. An alternative source might arise from slight variations in the geometry of the lower crustal bodies.

The second cross-section, Section 9, is located perpendicular to the Central FZ (Fig. 7 and 9). It marks the boundary of the

300   TNDR 3 package, which cross-cuts into the TNDR 4 package, accompanied by a change of orientation of the dip direction (Thomas et al., 2022).

In general, the Moho boundary shallows from 14 km depth in the SE to 11 km depth in the offshore part in the NW (Fig. 9c+d). The reflection of the Moho boundary is not as sharp as in Section 5. Prominent reflections are evident in the center of the profile at the 25 km marker, related to a sudden deepening of the Moho boundary, and in the SE, seen as a small shallowing

305   of the Moho boundary from 15 to 13 km depth (Fig. 9d). In the lower crust, a constant density of 2.93-2.94 g/cm³ characterizes the central and eastern part. The sharp density gradient towards the TNDR 5 package is maintained, which is confirmed by lower crustal reflectors, probably related to the base of the TNDR 5 (Fig. 9d). The western part is modelled as a constant lower crustal body C1 with a density of 2.88 g/cm³, similar to the TNDR 5 package. A long wavelength anomaly in the gravity data causes a slight worse mismatch of 1.4 mGal and might reflect a regional trend (Fig. A4).

310   The main susceptibility contrast is located at the western edge of the TNDR 5 package between the 20-25 km markers, modelled as a jump from 0.139 SI in the TNDR package to 0.195 SI in the western lower crustal body C1. Susceptibilities in the eastern part mainly follow the average values of the clustering and fit the magnetic data (Fig. 9b). Interestingly, the main susceptibility gradient of the section is located in the western part of the TNDR 5 package between the 18-25 km markers, whereas the main density gradient marks the eastern part of the TNDR 5 package, located between the 25-30 km markers. This

315   might indicate different petrological properties in the vicinity of the TNDR-B 5 surface.
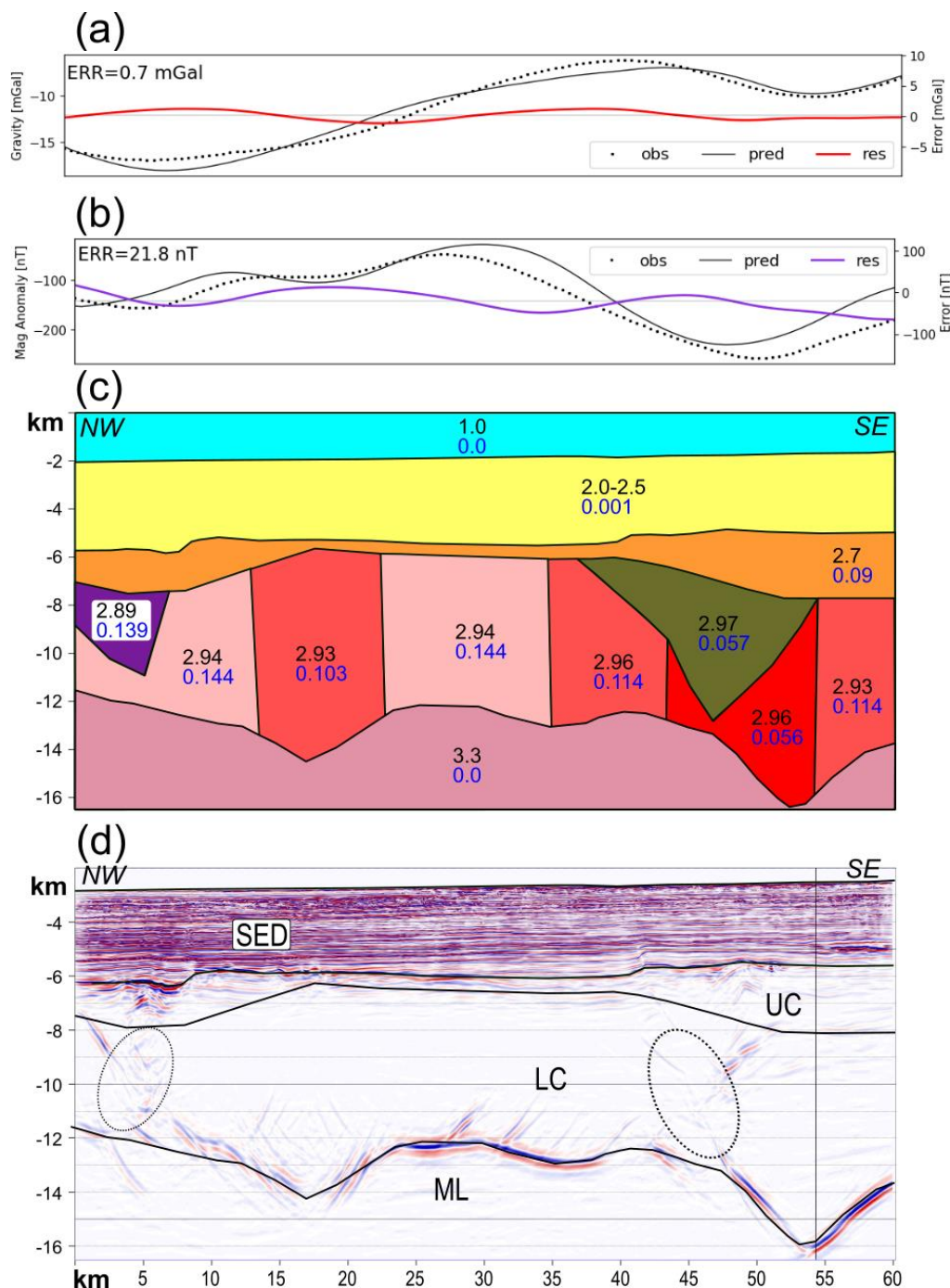
Figure 8: Section 5 – 2D profile across the Central and Ascension FZ. (a) Observed, predicted and residual gravity data. (b) Observed, predicted and residual magnetic data. The errors denote the standard deviation of the residual data. (c) IGMAS cross-section with densities in g/cm³ (black numbers) and susceptibilities (blue numbers) of the lower crust. The lower crust is split in several blocks, as obtained by cluster analysis. For coherent blocks, the density and susceptibility are allowed to vary within the standard deviation values (Table 2). TNDR structures are highlighted by violet (TNDR 3) and green colour (TNDR 5). (d) Seismic dip-line with interpreted horizons, taken from Thomas et al. (2022). SED= Sediments, UC= Upper Crust, LC= Lower Crust, ML= Mantle Lithosphere. Dashed ellipses mark TNDR-B 3 on the left and TNDR-B 5 on the right.

320
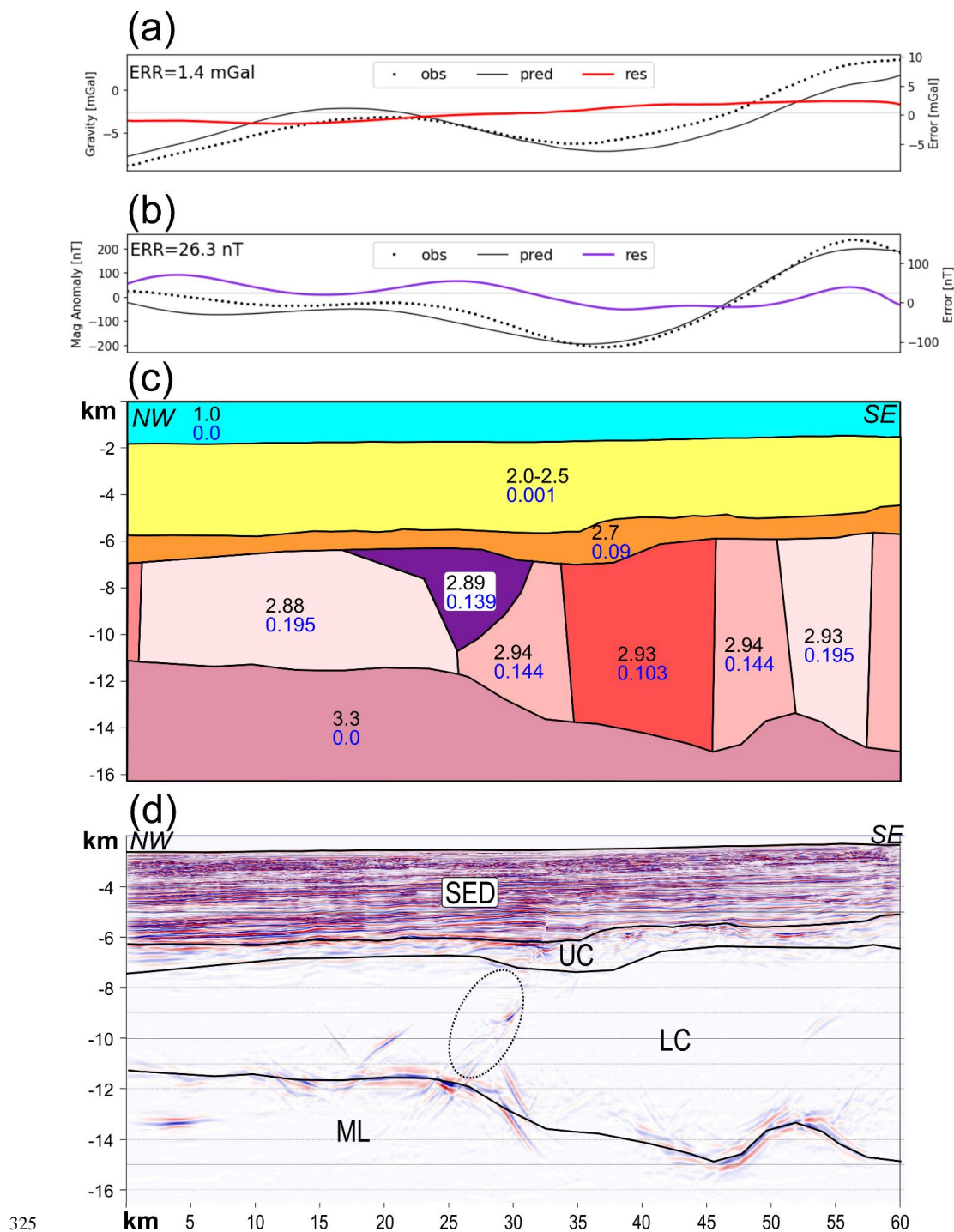
Figure 9: Section 9 – 2D profile across the Central FZ. (a) Observed, predicted and residual gravity data. (b) Observed, predicted and residual magnetic data. The errors denote the standard deviation of the residual data. (c) IGMAS cross-section with densities in g/cm³ (black numbers) and susceptibilities (blue numbers) of the lower crust. For coherent blocks, the density and susceptibility are allowed to vary within the standard deviation values (Table 2). TNDR 3 package is highlighted by violet colour. (d) Seismic dip-line with interpreted horizons, taken from Thomas et al. (2022). SED= Sediments, UC= Upper Crust, LC= Lower Crust, ML= Mantle Lithosphere. Dashed ellipses mark TNDR-B 3.

5 Discussion

5.1 High magnetization in the lower crust

While the modelled densities are within the range of lower crustal materials, the modelled susceptibilities are higher than
335   expected (e.g., Dentith and Mudge, 2018). For example, the crust along the Mid-Norwegian continental margin crust is of
similar age, but shows susceptibilities up to maximum 0.075 SI in the lower crust (Maystrenko et al., 2018). Another study
reports maximum susceptibility of 0.06 SI for mafic intrusions in the Barents Sea (Fichler and Pastore, 2022), which is less
than half the maximum susceptibility of our model.

We see two reasons for the high susceptibilities in our model: first, there are additional magnetic sources outside the lower
340   crust that the model is not accounting for. We have shown in the results that this scenario is not preferred, because the volume
of the upper crust and possible volcanics within the sedimentary section is not sufficient to account for the remaining signal.
Second, the contribution of remanent magnetization to the observed magnetic anomalies plays a more significant role than
expected.

The fundamental problem for modelling remanent magnetization is that there are no samples of the crust available. Generally,
345   direct measurements via scientific drillholes are very expensive, and if executed, they mostly do not penetrate deeper than Top
Oceanic Crust. Remanent magnetization of sheeted dike complexes can also be investigated with ROVs, if oceanic crust is
directly exposed at the seafloor. Naturally, these studies are mainly focussed on spreading centers of active mid-oceanic ridges,
where sedimentation has not yet buried the crustal material underneath (e.g., Varga et al., 2008).

A further complication is that the eastern Gulf of Guinea is located in the CNS, where globally there is no evidence for polar
350   reversal, leaving no signatures in the remanent magnetization. However, global satellite magnetic models imply enhanced
remanent magnetization over the CNS, which was attributed to increased main field intensity (LaBrecque and Raymond, 1985).
In a subsequent global study, the source depths to satisfy the amount of magnetization required to fit the satellite magnetic
data was located in the deeper part of the oceanic crust (Dyment and Arkani-Hamed, 1998). Even though the wavelength
characteristics of the satellite data differs from the magnetic data acquired in the eastern Gulf of Guinea and a simplified crustal
355   model with unique layers was used, there seems to be a significant contribution of remanent magnetization in the lower crust
of CNS regime (Dyment and Arkani-Hamed, 1998; Hemant and Maus, 2005).

Geomagnetic polarity during the CNS was oriented in normal direction (Ogg, 2020), even though short reversal events may
have existed (Yoshimura, 2022). Hence, the presence of remanent magnetization in our study area would amplify the magnetic
signal in the same direction. In other words, parts of the modelled total magnetization can be regarded as remanent. The
360   Koenigsberger Ratio Q, which is the ratio between remanent and induced magnetization, can be used to scale the modelled
susceptibility. Assuming Q=3, a typical value for basalt or gabbro (Clark, 1997), would replace 75 % of the modelled
susceptibility in the lower crust with remanent magnetization.

We apply $Q=3$ to the lower crust and investigate whether the modelled features are maintained (Fig. 10). For this test, we
change the input data set to Total Field Intensity (Fig. A1), because modelling RTP data assumes that remanent magnetization
365   is negligible. For Section 5 the lower crustal susceptibilities vary between 0.014-0.036 SI (Fig. 10b), which is in the expected
range for basaltic or gabbroic material (Clark and Emerson, 1991). The error of the residual magnetic data of the cross-section
(Fig. 10a) is similar to the previous case. The same holds for the gridded residual magnetic data (Fig. 10c vs. Fig. 10d).
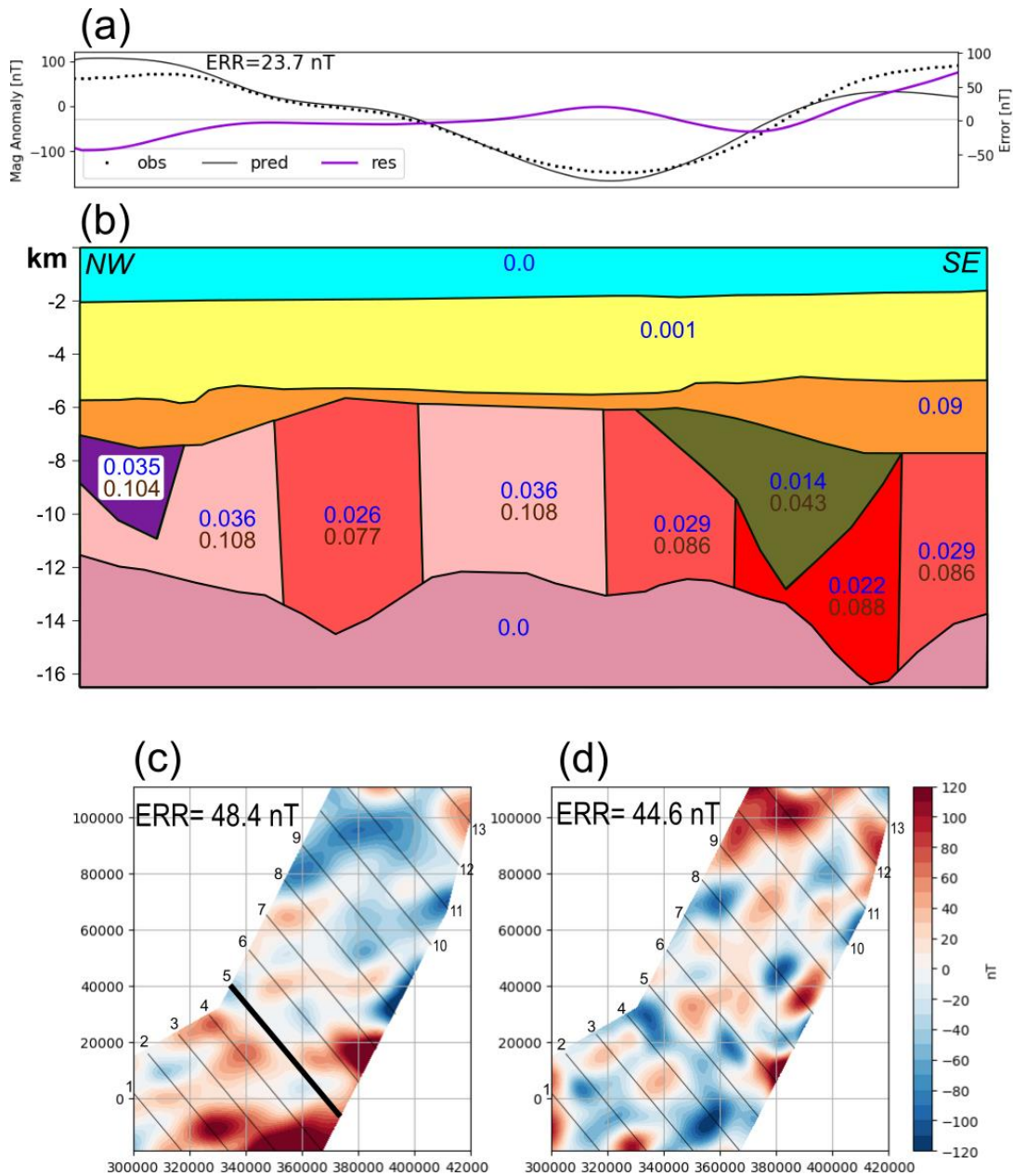
Figure 10: Section 5 – 2D profile across the Central and Ascension FZ. The geometry of the model is similar to Fig. 8. (a) Observed, predicted and residual magnetic data using TFI data. (b) Cross-section with susceptibilities only. Lower crust is modelled with induced (blue values) and remanent magnetization (brown values). To fit the trend of the data, the total susceptibility of cluster C5 (red block) was increased from 0.056 to 0.088 SI. (c) Residual magnetic data of the study area, assuming induced and remanent magnetization and using TFI data as input. (d) Residual magnetic data, assuming induced magnetization only and using RTP data as input. Regular numbers indicate the labels of the cross-sections. Thick black line highlights Section 5.

There are two main reasons why the error of the residual magnetic data is not reduced when applying remanent magnetization to the model. First, a constant value of Q scales the absolute susceptibilities of the lower crust. In this case, the susceptibility contrasts between the different lower crustal segments are maintained. Second, the paleo-inclination of the magnetic field was different when the crust was magnetized in Cretaceous. Applying paleo-inclination to the model requires a rescaling of the

380 modelled susceptibilities, causing that the susceptibility contrasts between the different lower crustal segments are not maintained. However, introducing a variable Q and paleo-inclination of the magnetic field require petrological samples. Otherwise, uncertainties of the modelled susceptibilities will increase. Therefore, the model we have constructed accounting for remanent magnetization in the same direction as the main field with a constant Q can readily be applied to structural interpretation and relation to the tectonic regime.

5.2 Implications for metamorphic conditions

385 The lower crustal properties might not only reflect in-situ tectonics, but also far-field stresses related to the CVL. For the offshore origin of the CVL various deep seated sources have been proposed (e.g., Reusch et al., 2011; Milelli et al., 2012; Celli et al., 2020). However, seismic data several hundred km northwest of this study area in the offshore territory of Equatorial Guinea suggests that compressional and strike-slip tectonics in the oceanic crust could have contributed to the formation of the CVL (Lawrence et al., 2017). In this light, the fracture zones we have imaged in our study area could have acted as a

390 conduit for the CVL to reduce the lower crustal susceptibility. However, the clear spatial correlation between the low susceptibility and the seismically mapped TNDR packages suggest a different picture.

Abyssal hills facies overlying the fracture zones and sealing the TNDR packages date them to be prior to the end of ridge based volcanic processes (Thomas et al., 2022) and significantly older than the Oligocene CVL (Adams, 2022). Altered susceptibility as a post accretion feature from the CVL therefore can be ruled out. Instead, the model demonstrates a statistically

395 significant difference between oceanic crust generated through transform processes in the TNDR packages (Thomas et al., 2022) and the similar aged 'typical' oceanic crust generated at adjacent spreading ridges.

We suggest that the variations of density and susceptibility reflect different stages during accretion and evolution of oceanic crust, which are closely related to varying pressure (P) and temperature (T) conditions. The density and magnetic properties of rocks are caused by a combination of hydrothermal alteration during crustal formation, followed by a change of compaction

400 and metamorphism after sediment burial (e.g., Honnorez, 2003). However, our results suggest that the strength of hydrothermal alteration and subsequent metamorphic processes are highly variable between OFZ and abyssal hills type crust.

To estimate the PT conditions of the crust within the study area at the time of accretion, we assume a source depth of 3-10 km below sea level once the sediment pile has been removed. With a typical lithostatic gradient of 0.03 GPa/km (Allen and Allen, 2013) and a temperature gradient between 3 and 5 °C per 100 m, in-situ conditions of 0.09-0.3 GPa and a temperature range

405 between 150-350° C can be expected. These PT conditions are typical for Zeolite and Prehnite-Pumpellyite Facies (see e.g., Fig. 2.8 in Winter, 2001), which are characterized by hydrothermal alteration of oceanic crust around mid-ocean ridges (Mevel, 1981).

At mid-oceanic ridges, hydrothermal alteration might cause serpentinization of mantle peridotites (e.g., Rouméjon and Cannat, 2014). Serpentinization preferably occurs underneath slow spreading ridges in a temperature range between 300-500° C

410 (Mével, 2003). While the inverted susceptibility and the temperature range here would allow serpentinization as a process to alter the lower crust, the inverted density in the area of the Ascension and Central FZ is too high to represent serpentinized upper mantle peridotite, which is in the lower density range of rock-forming minerals (Dentith and Mudge, 2018). Therefore, serpentinization is an unlikely process of lower crustal alteration.

The above maximum PT values would allow increased metamorphism with possible transition even to the lower limit of

415 Greenschist Facies. The deep crust in combination with high densities and low magnetization (Clusters C4 and C5) indicate that some portion of the lower crust beneath the Ascension and Central FZ could have reached PT conditions of Greenschist Facies. Even though metamorphic conditions for Greenschist Facies are typically reached during mountain building processes, samples of seafloor basalts in the Atlantic were attributed to this facies (Fox and Opdyke, 1973). These rocks represent mineral

420   transformations during hydrothermal activity, rather than deformed and schistosed rocks, which are typical for regional metamorphism (Frisch et al., 2022).

The increasing PT conditions and the subsequent change of metamorphic facies cause a change of the magnetization of the oceanic crust, which can be traced in a diagram of induced magnetism: proceeding from Zeolite Facies, basaltic material will lose magnetic properties due to oxidation of iron-rich titanomagnetites (see Fig. 3.48d in Dentith and Mudge, 2018). The observed low susceptibilities for the fracture zones probably reflect increasing temperatures, which are further increased

425   relative to the adjacent crust, accompanied by a change of metamorphic facies. This is predicted by transform fault finite element models of Behn et al. (2007) as well as by the viscoplastic numerical model of Grevemeyer et al. (2021) in relation to mantle upwelling in areas of oblique extension within the ridge-transform inside corner. Furthermore, the TNDR geometries within this dataset have been interpreted as related to the emplacement of a thick series of extrusive lava flows within the ridge-transform inside corner, necessitating a higher heat flow in relation to the adjacent crust (Thomas et al., 2022).

430   The evolving PT conditions within the inside corner of the ridge-transform segment could change the density and magnetic properties during crustal accretion. This observation is in agreement with recent studies that describe the non-conservative character of ridge-transform fault segments (Grevemeyer et al., 2021; Thomas et al., 2022). However, if the observed density and magnetic properties along fracture zone are a special case for São Tomé or rather a generalized mechanism needs to be investigated in future studies.

435   6 Conclusions

Combining shipborne potential field data with high resolution 3D seismic data highlights the variable structure of the crust offshore São Tomé and Príncipe. We have presented models of inverted density and susceptibility that show the special character of buried oceanic fracture zones in the study area. The fracture zones and their associated intra-crustal reflectors, previously identified as TNDR sequences, are characterized by a high-density and low-magnetic lower crust that clearly

440   distinguish them from the surrounding tectonic fabric.

The derived densities and susceptibilities are typical for metamorphic rocks and indicate increasing pressure and temperature conditions accompanied by a change of metamorphic facies. In a broader perspective, the evolving temperature and pressure conditions within the inside corner of the ridge-transform segment could change the density and magnetic properties during crustal accretion. These observations imply enhanced tectonic and thermal activity during the formation of transform faults

445   and is in agreement with previous models that exhibit the non-conservative character of ridge-transform intersections (Grevemeyer et al., 2021; Thomas et al., 2022).

Appendices
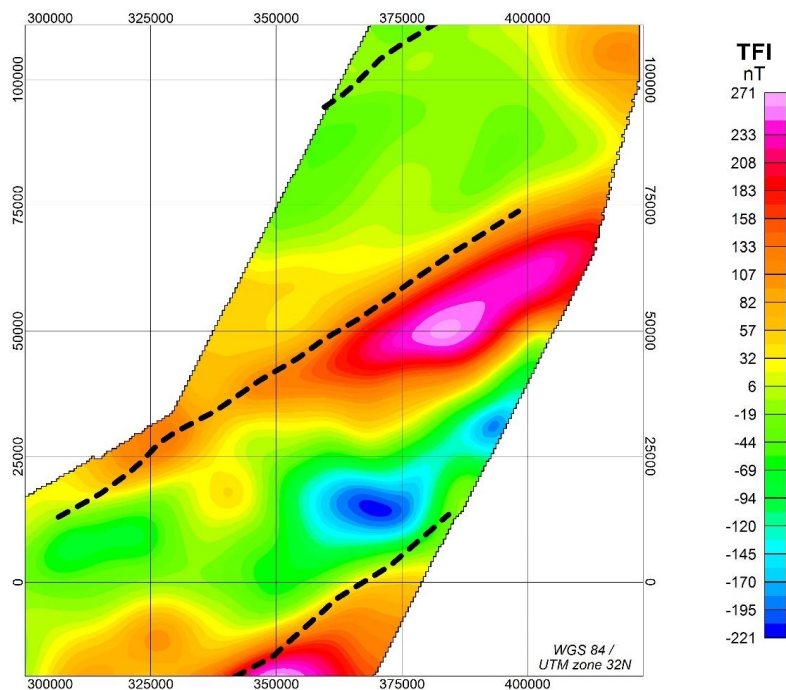
450   **Figure A1: Total Field Intensity (TFI) data of the study area. Dashed line shows fracture zones.**

Cluster No.	1	2	3	4	5
TNDR	Medium ρ	Medium ρ	Low ρ	Medium ρ	High ρ
Unit	Medium χ	High χ	Medium χ	Low χ	Very low χ
1	79.1		0.2		20.7
2	97.5				2.5
3	59.8			6.9	33.3
4	90.4		8.2		1.4
5	22.5		0.1	54.6	22.8
Total TNDR	55.8	0.0	1.5	20.8	21.7
Total Data	61.7	3.9	13.7	11.5	9.2

Table A1: Relative distribution of the individual TNDR packages in the different clusters. Values are in %. The sum of each row equals 100 %. Total TNDR represents the weighted average distribution of all TNDRs in the respective cluster domain. Total Data shows the distribution of the entire data set. For example, TNDR 5 show a relative high abundance for Cluster No. 4, compared to the TNDR average. ρ=density, χ=susceptibility.

455
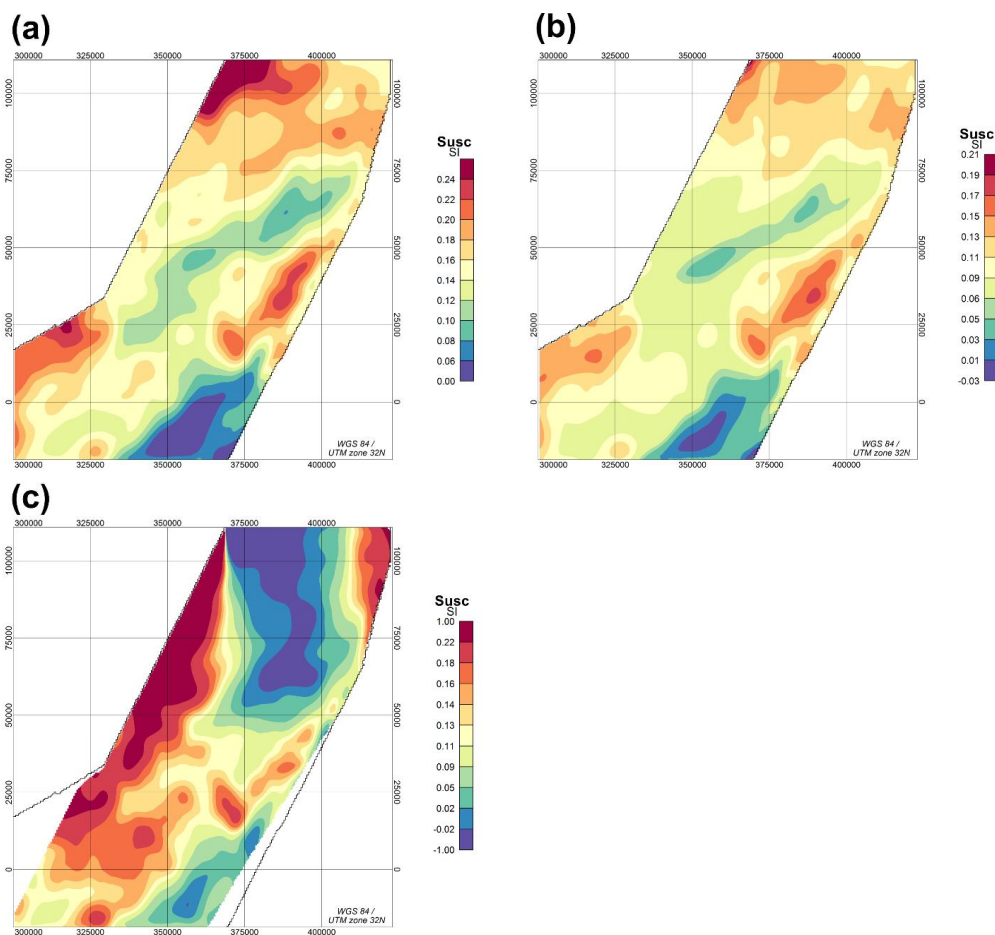
Figure A2: Inverted susceptibilities of the lower crust for different model assumptions. (a) Susceptibility of the lower crust, equivalent to Fig. 4b, (b) Susceptibility for the entire crust, without differentiation in upper and lower crust, (c) Susceptibility for the lower crust, but using TFI data as input.

460
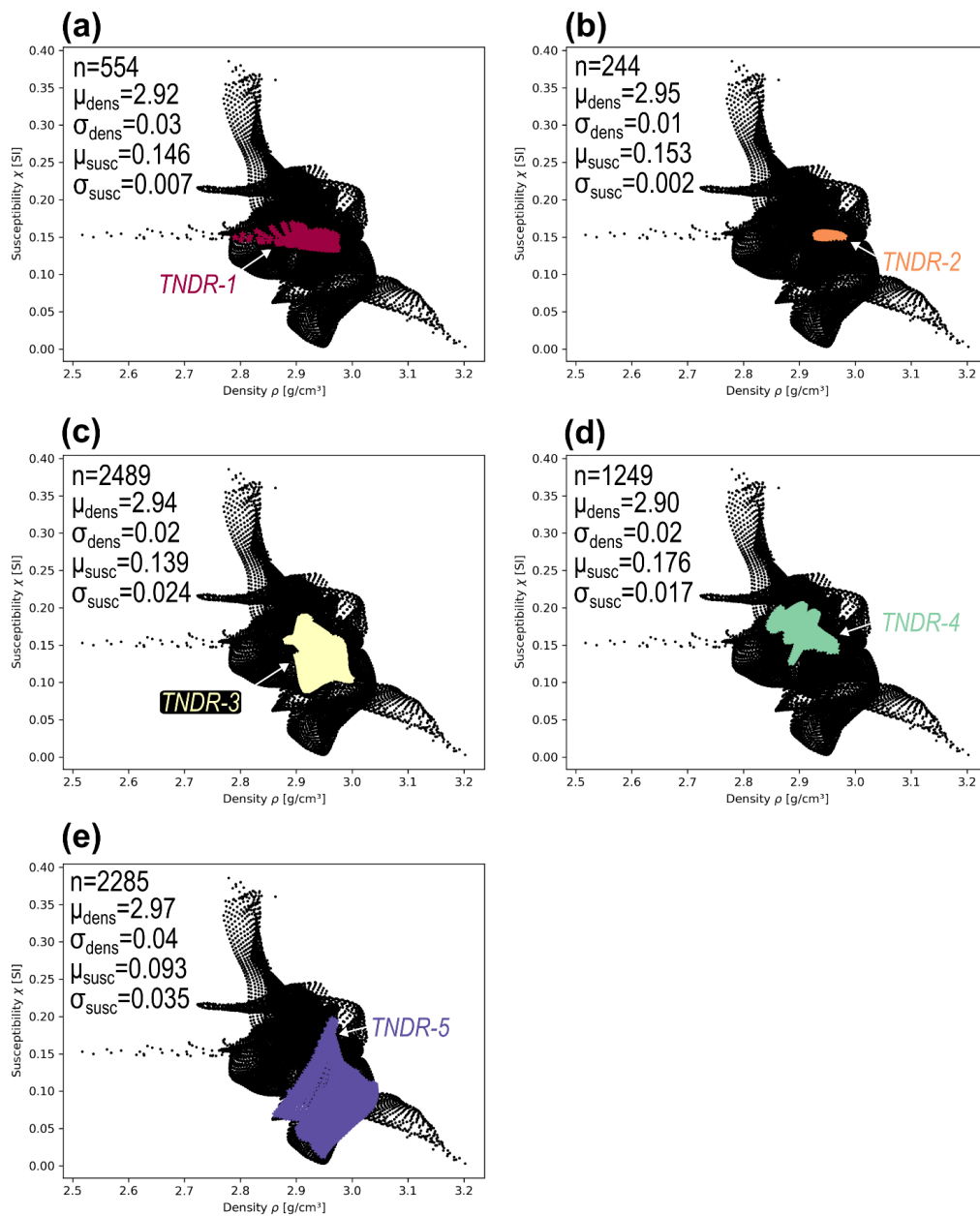
Figure A3: Diagram showing the distribution of the gridded inverted density vs. the gridded inverted susceptibility (black dots). Coloured points mark the distribution of the values within the individual TNDR geometry. Each plot contains information on number of grid points n, mean density μ$_{dens}$, mean susceptibility μ$_{susc}$, as well as standard deviation of density σ$_{dens}$ and standard deviation of susceptibility σ$_{susc}$. (a) TNDR-1, (b) TNDR-2, (c) TNDR-3, (d) TNDR-4, (e) TNDR-5.

465
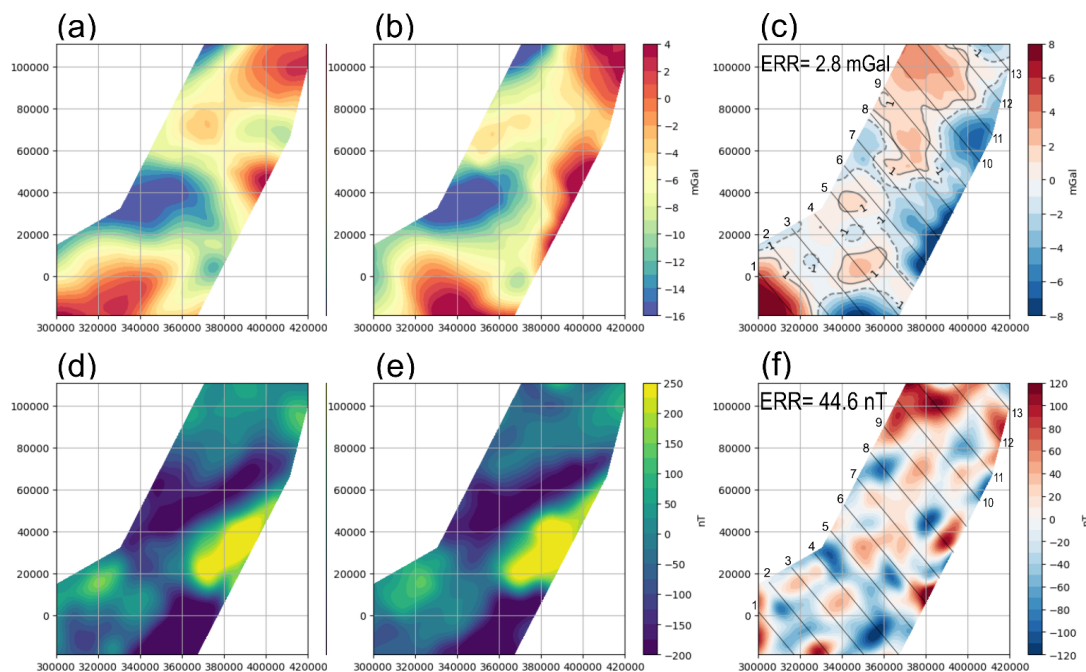
Figure A4: Data and residuals of the final model. Top row shows gravity data, bottom row magnetic data. First column shows observed data, second column calculated data of the model, third column the residual between these two. (a) Observed gravity, (b) calculated gravity, (c) residual gravity, (d) observed magnetic, (e) calculated magnetic, (f) residual magnetic. The relative high error in the residual is a consequence of the limited number of bodies and the given range of density and susceptibility values obtained in the clustering.

470

Code availability

The modelled densities and susceptibilities of the lower crust have been produced with the software Oasis Montaj and IGMAS+

475   (Anikiev et al., 2020). A code that reproduces the results of the clustering is available for reviewer and editor only, but will be

made available for the public after publication of the manuscript.

Data availability

The gravity and magnetic data is a proprietary survey acquired by CGG in 2017 for the Oil and Gas exploration companies

Kosmos Energy, Galp and Shell Global. Under the STP petroleum law and the production sharing agreements for Blocks 6

480   and 11, ANP-STP as the oil & gas regulator is the ultimate data owner. All the aforementioned parties are legally bound to

keep this data confidential. Requests for data access can be made through Shell Global via Myron Thomas

(Myron.thomas@shell.com).

Author contribution

PH drafted the manuscript and constructed the model. MT prepared the geotiffs and lead the interpretation of the seismic dip

485   lines. CH assisted in the tectonic interpretation of the model. AS helped with processing and interpretation of the potential

field data. JE helped set up the IGMAS model and assisted in conceptualization of the manuscript. JvI assisted in data

acquisition and cared about stakeholder interests. All authors read and commented on the draft manuscript.

Competing interests

The contact author has declared that none of the authors has any competing interests.

490   **Acknowledgments**

We would like to thank Shell International Exploration and Production and our joint venture partners Galp São Tomé and Príncipe Unipessoal, and the regulator, the Agência Nacional do Petróleo de São Tomé e Príncipe, for granting permission to publish this work. This paper would not have been possible without the exceptional subsurface data. We owe special thanks to as the Agência Nacional do Petróleo de São Tomé e Príncipe, regulator and data owner, who have kindly granted us
495   permission to use the gravity and magnetics data for this paper. We are further thankful for CGG Multiphysics, who acquired and processed the shipborne potential field data and gave us insights into the acquisition and processing report. We would also like to express our gratitude to Sabine Schmidt from Kiel University for her assistance while working with IGMAS+ software.

500   # References

Adams, A.: Insights Into the Source of Magmatic Hot-Lines: Forty Years of Geophysical Studies of the Cameroon Volcanic Line, Front. Earth Sci., 10, https://doi.org/10.3389/feart.2022.838993, 2022.

Allen, P. A. and Allen, J. R.: Basin analysis: Principles and applications, 3. ed., Wiley-Blackwell, Chichester, 619 pp., 2013.

Anikiev, D., Götze, H.-J., Meeßen, C., Plonka, C., Scheck-Wenderoth, M., and Schmidt, S.: IGMAS+: Interactive Gravity and Magnetic
505   Application System, GFZ Data Services, 2020.

Antobreh, A. A., Faleide, J. I., Tsikalas, F., and Planke, S.: Rift–shear architecture and tectonic development of the Ghana margin deduced from multichannel seismic reflection and potential field data, Marine and Petroleum Geology, 26, 345–368, https://doi.org/10.1016/j.marpetgeo.2008.04.005, 2009.

Behn, M. D., Boettcher, M. S., and Hirth, G.: Thermal structure of oceanic transform faults, Geol, 35, 307,
510   https://doi.org/10.1130/G23112A.1, 2007.

Catalán, M., Negrete-Aranda, R., Martos, Y. M., Neumann, F., Santamaría, A., and Fuentes, K.: On the intriguing subject of the low amplitudes of magnetic anomalies at the Powell Basin, Front. Earth Sci., 11, https://doi.org/10.3389/feart.2023.1199332, 2023.

Celli, N. L., Lebedev, S., Schaeffer, A. J., Ravenna, M., and Gaina, C.: The upper mantle beneath the South Atlantic Ocean, South America and Africa from waveform tomography with massive data sets, Geophysical Journal International, 221, 178–204,
515   https://doi.org/10.1093/gji/ggz574, 2020.

Clark, D. A. and Emerson, J. B.: Notes On Rock Magnetization Characteristics In Applied Geophysical Studies, Exploration Geophysics, 22, 547–555, https://doi.org/10.1071/EG991547, 1991.

Clark, D.: Magnetic petrophysics and magnetic petrology: Aids to geological interpretation of magnetic surveys, 17, 83–104, 1997.

Dentith, M. and Mudge, S. T.: Geophysics for the Mineral Exploration Geoscientist, Cambridge University Press, 2018.

520   Dyment, J. and Arkani-Hamed, J.: Contribution of lithospheric remanent magnetization to satellite magnetic anomalies over the world's oceans, J. Geophys. Res., 103, 15423–15441, https://doi.org/10.1029/97JB03574, 1998.

Fichler, C. and Pastore, Z.: Petrology of the crystalline crust in the southwestern Barents Sea inferred from geophysical data, NJG, https://doi.org/10.17850/njg102-2-2, 2022.

Fox, P. J. and Opdyke, N. D.: Geology of the oceanic crust: Magnetic properties of oceanic rocks, J. Geophys. Res., 78, 5139–5154,
525   https://doi.org/10.1029/JB078i023p05139, 1973.

Frisch, W., Meschede, M., and Blakey, R. C.: Plate Tectonics: Continental Drift and Mountain Building, 2nd ed., Springer Textbooks in Earth Sciences, Geography and Environment Ser, Springer International Publishing AG, Cham, 247 pp., 2022.

Götze, H. -J. and Lahmeyer, B.: Application of three-dimensional interactive modeling in gravity and magnetics, GEOPHYSICS, 53, 1096–1108, https://doi.org/10.1190/1.1442546, 1988.

530 Granot, R., Dyment, J., and Gallet, Y.: Geomagnetic field variability during the Cretaceous Normal Superchron, Nature Geosci, 5, 220–223, https://doi.org/10.1038/ngeo1404, 2012.

Gregg, P. M., Lin, J., Behn, M. D., and Montési, L. G. J.: Spreading rate dependence of gravity anomalies along oceanic transform faults, Nature, 448, 183–187, https://doi.org/10.1038/nature05962, 2007.

Grevemeyer, I., Rüpke, L. H., Morgan, J. P., Iyer, K., and Devey, C. W.: Extensional tectonics and two-stage crustal accretion at oceanic

535 transform faults, Nature, 591, 402–407, https://doi.org/10.1038/s41586-021-03278-9, 2021.

Guo, Z., Liu, S., Rüpke, L., Grevemeyer, I., Morgan, J. P., Lange, D., Ren, Y., and Tao, C.: Disparate crustal thicknesses beneath oceanic transform faults and adjacent fracture zones revealed by gravity anomalies, Geol, 51, 300–304, https://doi.org/10.1130/G50429.1, 2023.

Harlan, R. B.: Eotvos corrections for airborne gravimetry, J. Geophys. Res., 73, 4675–4679, https://doi.org/10.1029/JB073i014p04675, 1968.

540 Heine, C., Zoethout, J., and Müller, R. D.: Kinematics of the South Atlantic rift, Solid Earth, 4, 215–253, https://doi.org/10.5194/se-4-215-2013, 2013.

Hemant, K. and Maus, S.: Geological modeling of the new CHAMP magnetic anomaly maps using a geographical information system technique, J. Geophys. Res., 110, https://doi.org/10.1029/2005JB003837, 2005.

Honnorez, J.: Hydrothermal alteration vs. ocean-floor metamorphism. A comparison between two case histories: the TAG hydrothermal

545 mound (Mid-Atlantic Ridge) vs. DSDP/ODP Hole 504B (Equatorial East Pacific), Comptes Rendus Geoscience, 335, 781–824, https://doi.org/10.1016/j.crte.2003.08.009, 2003.

Keen, C. and Tramontini, C.: A Seismic Refraction Survey on the Mid-Atlantic Ridge, Geophysical Journal International, 20, 473–491, https://doi.org/10.1111/j.1365-246X.1970.tb06087.x, 1970.

LaBrecque, J. L. and Raymond, C. A.: Seafloor spreading anomalies in the Magsat field of the North Atlantic, J. Geophys. Res., 90, 2565–

550 2575, https://doi.org/10.1029/JB090iB03p02565, 1985.

Lawrence, S. R., Beach, A., Jackson, O., and Jackson, A.: Deformation of oceanic crust in the eastern Gulf of Guinea: role in the evolution of the Cameroon Volcanic Line and influence on the petroleum endowment of the Douala-Rio Muni Basin, SP, 438, 7–26, https://doi.org/10.1144/SP438.7, 2017.

Lee, D.-C., Halliday, A. N., Fitton, J., and Poli, G.: Isotopic variations with distance and time in the volcanic islands of the Cameroon line:

555 evidence for a mantle plume origin, Earth and Planetary Science Letters, 123, 119–138, https://doi.org/10.1016/0012-821X(94)90262-3, 1994.

Li, X.: Magnetic reduction-to-the-pole at low latitudes: Observations and considerations, The Leading Edge, 27, 990–1002, https://doi.org/10.1190/1.2967550, 2008.

Lizarralde, D., Gaherty, J. B., Collins, J. A., Hirth, G., and Kim, S. D.: Spreading-rate dependence of melt extraction at mid-ocean ridges

560 from mantle seismic refraction data, Nature, 432, 744–747, https://doi.org/10.1038/nature03140, 2004.

Longman, I. M.: Formulas for computing the tidal accelerations due to the moon and the sun, J. Geophys. Res., 64, 2351–2355, https://doi.org/10.1029/JZ064i012p02351, 1959.

Lösing, M., Moorkamp, M., and Ebbing, J.: Joint inversion based on variation of information—a crustal model of Wilkes Land, East Antarctica, Geophysical Journal International, 232, 162–175, https://doi.org/10.1093/gji/ggac334, 2022.

565 Marjanović, M., Singh, S. C., Gregory, E. P. M., Grevemeyer, I., Growe, K., Wang, Z., Vaddineni, V., Laurencin, M., Carton, H., La Gómez de Peña, L., and Filbrandt, C.: Seismic Crustal Structure and Morphotectonic Features Associated With the Chain Fracture Zone and Their Role in the Evolution of the Equatorial Atlantic Region, Journal of geophysical research. Solid earth, 125, e2020JB020275, https://doi.org/10.1029/2020JB020275, 2020.

Matthews, K. J., Müller, R. D., Wessel, P., and Whittaker, J. M.: The tectonic fabric of the ocean basins, J. Geophys. Res., 116,

570 https://doi.org/10.1029/2011JB008413, 2011.

Maystrenko, Y. P., Gernigon, L., Nasuti, A., and Olesen, O.: Deep structure of the Mid-Norwegian continental margin (the Vøring and Møre basins) according to 3-D density and magnetic modelling, Geophysical Journal International, 212, 1696–1721, https://doi.org/10.1093/gji/ggx491, 2018.

575   Mevel, C.: Occurrence of pumpellyite in hydrothermally altered basalts from the Vema fracture zone (mid-Atlantic ridge), Contr. Mineral. and Petrol., 76, 386–393, https://doi.org/10.1007/BF00371480, 1981.

Mével, C.: Serpentinization of abyssal peridotites at mid-ocean ridges, Comptes Rendus Geoscience, 335, 825–852, https://doi.org/10.1016/j.crte.2003.08.006, 2003.

Meyers, J. B., Rosendahl, B. R., Harrison, C. G., and Ding, Z.-D.: Deep-imaging seismic and gravity results from the offshore Cameroon Volcanic Line, and speculation of African hotlines, Tectonophysics, 284, 31–63, https://doi.org/10.1016/s0040-1951(97)00173-x, 1998.

580   Milelli, L., Fourel, L., and Jaupart, C.: A lithospheric instability origin for the Cameroon Volcanic Line, Earth and Planetary Science Letters, 335-336, 80–87, https://doi.org/10.1016/j.epsl.2012.04.028, 2012.

Ogg, J. G.: Geomagnetic Polarity Time Scale, in: Geologic Time Scale 2020, Elsevier, 159–192, https://doi.org/10.1016/B978-0-12-824360-2.00005-X, 2020.

Olive, J.-A., Behn, M. D., Ito, G., Buck, W. R., Escartín, J., and Howell, S.: Sensitivity of seafloor bathymetry to climate-driven fluctuations
585   in mid-ocean ridge magma supply, Science (New York, N.Y.), 350, 310–313, https://doi.org/10.1126/science.aad0715, 2015.

Osorio-Granada, A. M., Jigena-Antelo, B., Vidal Pérez, J. M., Hernández-Pardo, O., León-Rincón, H., and Muñoz-Pérez, J. J.: Potential fields modeling for the Cayos Basin (Western Caribbean Plate): Implications in basin crustal structure, Marine Geology, 449, 106819, https://doi.org/10.1016/j.margeo.2022.106819, 2022.

Parker, R. L.: The Rapid Calculation of Potential Anomalies, Geophysical Journal International, 31, 447–455, https://doi.org/10.1111/j.1365-
590   246X.1973.tb06513.x, 1973.

Reusch, A. M., Nyblade, A. A., Tibi, R., Wiens, D. A., Shore, P. J., Bekoa, A., Tabod, C. T., and Nnange, J. M.: Mantle transition zone thickness beneath Cameroon: evidence for an upper mantle origin for the Cameroon Volcanic Line, Geophysical Journal International, 187, 1146–1150, https://doi.org/10.1111/j.1365-246X.2011.05239.x, 2011.

Rouméjon, S. and Cannat, M.: Serpentinization of mantle-derived peridotites at mid-ocean ridges: Mesh texture development in the context
595   of tectonic exhumation, Geochem Geophys Geosyst, 15, 2354–2379, https://doi.org/10.1002/2013GC005148, 2014.

Rundquist, D. and Sobolev, P.: Seismicity of mid-oceanic ridges and its geodynamic implications: a review, Earth-Science Reviews, 58, 143–161, https://doi.org/10.1016/S0012-8252(01)00086-1, 2002.

Schlindwein, V. and Schmid, F.: Mid-ocean-ridge seismicity reveals extreme types of ocean lithosphere, Nature, 535, 276–279, https://doi.org/10.1038/nature18277, 2016.

600   Seton, M., Müller, R. D., Zahirovic, S., Williams, S., Wright, N. M., Cannon, J., Whittaker, J. M., Matthews, K. J., and McGirr, R.: A Global Data Set of Present-Day Oceanic Crustal Age and Seafloor Spreading Parameters, Geochem Geophys Geosyst, 21, https://doi.org/10.1029/2020GC009214, 2020.

Somoza, L., Medialdea, T., González, F. J., Machancoses, S., Candón, J. A., Cid, C., Calado, A., Afonso, A., Pinto Ribeiro, L., Blasco, I., Albuquerque, M., Asensio-Ramos, M., Bettencourt, R., Ignacio, C. de, López-Pamo, E., Ramos, B., Rincón-Tomás, B., Santofimia, E.,
605   Souto, M., Tojeira, I., Viegas, C., and Madureira, P.: High-resolution multibeam bathymetry of the northern Mid-Atlantic Ridge at 45–46° N: the Moytirra hydrothermal field, Journal of Maps, 17, 184–196, https://doi.org/10.1080/17445647.2021.1898485, 2021.

Stewart, I. C.: A simple approximation for low-latitude magnetic reduction-to-the-pole, Journal of Applied Geophysics, 166, 57–67, https://doi.org/10.1016/j.jappgeo.2019.04.021, 2019.

Thomas, M. F. H., Heine, C., van Itterbeeck, J., Ostanin, I., Seregin, A., Spaak, M., Morales, T., and Essink, T. O.: A New Model for the
610   Evolution of Oceanic Transform Faults Based on 3D Broadband Seismic Observations From São Tomé and Príncipe in the Eastern Gulf of Guinea, Geochem Geophys Geosyst, 23, https://doi.org/10.1029/2022GC010351, 2022.

Vaddineni, V. A., Singh, S. C., Grevemeyer, I., Audhkhasi, P., and Papenberg, C.: Evolution of the Crustal and Upper Mantle Seismic Structure From 0-27 Ma in the Equatorial Atlantic Ocean at 2° 43'S, Journal of geophysical research. Solid earth, 126, e2020JB021390, https://doi.org/10.1029/2020JB021390, 2021.

615   Varga, R. J., Horst, A. J., Gee, J. S., and Karson, J. A.: Direct evidence from anisotropy of magnetic susceptibility for lateral melt migration at superfast spreading centers, Geochem Geophys Geosyst, 9, https://doi.org/10.1029/2008GC002075, 2008.

Wessel, P., Matthews, K. J., Müller, R. D., Mazzoni, A., Whittaker, J. M., Myhill, R., and Chandler, M. T.: Semiautomatic fracture zone tracking, Geochem Geophys Geosyst, 16, 2462–2472, https://doi.org/10.1002/2015GC005853, 2015.

Wilson, J. T.: A New Class of Faults and their Bearing on Continental Drift, Nature, 207, 343–347, https://doi.org/10.1038/207343a0, 1965.

620   Wilson, P. G., Turner, J. P., and Westbrook, G. K.: Structural architecture of the ocean–continent boundary at an oblique transform margin through deep-imaging seismic interpretation and gravity modelling: Equatorial Guinea, West Africa, Tectonophysics, 374, 19–40, https://doi.org/10.1016/s0040-1951(03)00326-3, 2003.

Winter, J. D.: An introduction to igneous and metamorphic petrology, Prentice Hall, Upper Saddle River, NJ, 697 pp., 2001.

Yoshimura, Y.: The Cretaceous Normal Superchron: A Mini-Review of Its Discovery, Short Reversal Events, Paleointensity, Paleosecular
625   Variations, Paleoenvironment, Volcanism, and Mechanism, Front. Earth Sci., 10, https://doi.org/10.3389/feart.2022.834024, 2022.